IEEE Access
Multidisciplinary | Rapid Review | Open Access Journal

Received 6 July 2023, accepted 31 July 2023, date of publication 7 August 2023, date of current version 16 August 2023.

Digital Object Identifier 10.1109/ACCESS.2023.3303186

RESEARCH ARTICLE

Deep Learning-Based Phase Unwrapping Method

DONGXU LI[1] AND XIANMING XIE[2], (Member, IEEE)
[1]School of Automation, Guangxi University of Science and Technology, Liuzhou, Guangxi 545006, China
[2]School of Electronic Engineering, Guangxi University of Science and Technology, Liuzhou, Guangxi 545006, China

Corresponding author: Xianming Xie (xxmxgm@163.com)

This work was supported by the National Natural Science Foundation of China under Grant 62161003.

ABSTRACT A phase unwrapping method based on spatial and channel attention network is proposed to retrieve true phases from interferograms with various levels of noise. First, we propose a network that is suitable for unwrapping wrapped phase images. This network utilizes Deeplabv3+ as the backbone, adopts a serial-parallel atrous spatial pyramid pooling module, implements multi-scale skip connections between the encoder-decoder models, and fuses a convolutional block attention module. Second, datasets with different noise levels are used to train the network employing an existing noise level evaluation system, and the trained networks effectively handle the phase unwrapping for interferograms. Finally, the interferograms are unwrapped by the networks with the same noise level as the interferograms. The experimental results of phase unwrapping for interferograms fully verify the performance of this method.

INDEX TERMS Deep learning, noise evaluation, phase unwrapping, spatial and channel attention network.

I. INTRODUCTION

Phase Unwrapping (PU) technique has been widely used in holographic interferometry, interferometric synthetic aperture radar (INSAR), surface topography measurement, and nuclear magnetic resonance imaging [1], [2], [3], [4], [5], [6]. The measured phases (the so-called wrapped phases) obtained from the interferometric technique are wrapped into the range of $[-\pi, \pi)$, and the PU process recovers the true phases by adding an integer multiple of 2π to the wrapped pixels [7]. Traditional PU methods are roughly divided into path-following methods [8], [9], [10], [11], [12], [13], minimum-norm methods [14], [15], [16], [17], [18], and nonlinear filtering methods [19], [20], [21], [22], [23], [24]. Path-following methods include the quality-guided method [9], branch-cut method [10], and minimum cost flow methods [11], [12], and these methods can prevent errors from spreading among the entire image by setting appropriate integration paths. However, it is easy to result in the error propagation phenomenon along integration the paths in regions with low signal-to-noise ratio (SNR). In addition, the above methods are frequently time-consuming because of the time costs of finding an appropriate path. Minimum-norm methods include the unweighted least squares [14], [16] and weighted least squares [17] methods. Different from path-following methods, the unweighted and weighted least squares methods obtain the unwrapped results by establishing a suitable cost function for minimizing the difference between the phase gradients of the unwrapped phases and those of the wrapped phases. In addition, these methods demonstrate strong robustness and higher efficiency compared with the path-following methods in PU for interferograms with less noise. However, the dynamic range of the phase from interferograms with high phase dynamic deviation, may be reduced by these methods, which results in a loss of phase details. Nonlinear filtering methods include Kalman filter methods [19], [20], [21] and particle filter methods [22], [23]. These methods unwrap wrapped phase images by constructing a recursive estimation procedure under the Bayesian framework. Compared to the other two groups of methods, nonlinear filtering methods achieve stronger noise suppression and higher accuracy in PU for interferograms, but with higher time costs. In summary, above traditional methods can achieve popular solutions in many examples. However, for some applications that require high real-time, such as INSAR and nuclear magnetic resonance imaging, these methods still appear to be time-consuming to a great extent. Therefore, how to efficiently obtain true unwrapped phase from the wrapped phase is still an issue that needs to be solved. Deep learning (DL) techniques, which demonstrate

The associate editor coordinating the review of this manuscript and approving it for publication was Fabrizio Santi.

powerful feature representation and feature learning abilities, have gradually been applied to PU for interferograms, and several DL-based PU algorithms [25], [26], [27], [28], [29], [30], [31], [32], [33], [34], [35], [36] have also been proposed recently. Spoorthi et al. [25] transformed PU for interferograms into a semantic segmentation problem for wrapped fringe patterns by employing PhaseNet to predict the wrap-counts of wrapped pixels and obtained the unwrapped result after a postprocessing operation. Zhang et al. [26] and Zhang et al. [27] proposed robust PU procedures by exploiting SegNet and DeepLabv3 + to perform semantic segmentation for wrapped fringe patterns, respectively. Spoorthi et al. [28] proposed the approach referred to as the PhaseNet 2.0 by introducing a new loss function and dense blocks for the network to enhance the ability of resisting phase noise and class imbalance. In [29], the phase consistency delivered by the network is enhanced by introducing the coherence maps of interferograms as an input feature of the network. In [25], [26], [27], [28], and [29], inaccurate classification is prone to occur, resulting in an error of 2π integer multiples, when there is severe noise in interferograms. Accordingly, these methods sometimes need to be combined with various post-processing operations to remove the error of 2π integer multiples caused by the inaccurate classification, which increases technical complexity. Hence, the one-step PU techniques [30], [31], [32], [33] have proposed to obtain the unwrapped phase of wrapped pixels instead of its wrap-counts through constructing a direct mapping relationship between the wrapped phase and its true unwrapped phase using the network, and performing one-step PU on wrapped phase images without additional post-processing operations. Wang et al. [30] and Tian et al. [31] designed the one-step PU networks using classical UNET and UNET3+ as skeletons, respectively, to recover the true phase from noisy interferograms. Zhou et al. [32] proposed a conditional generative adversarial network called PU-GAN to execute one-step PU calculations, trying to accurately retrieve the unwrapped phase from INSAR interferograms. Meanwhile, some scholars combine deep learning with traditional algorithms to improve the robustness of the PU algorithms. BCNet [33] was combined with branch-cut approaches to improve the PU accuracy. Zhou et al. [34] employed PGNet to predict the phase gradient of pixels in different directions, and then the unwrapped results obtained via L^1-norm were shown to be better than those of conventional PU methods. Gao et al. [35] combined D-LinkNet with the UKF procedure to enhance the robustness of PU for interferograms. In addition, Vitale et al. [36] proposed the DL-based interferogram denoising approach to eliminate undesired phase noise presented in interferograms, without loss of phase details, through defining a suitable cost loss for the multi-objective network, which is beneficial for both reducing the difficulty of subsequent phase unwrapping procedures and obtaining the unwrapped phase of interferograms accurately. The above techniques have demonstrated popular results in some examples of PU for interferograms, and the advantage of efficiency in PU for interferograms are also demonstrated fully, compared with traditional methods. However, how to design a more effective and robust network architectures, build a fully representative data set for the networks, and design optimal cost functions for the networks to improve the robustness of the PU algorithms is still an issue that needs to be solved. This article focuses on robust network architecture design, attempting to construct a robust PU network, providing an effective solution for solving the PU problem under the framework of deep learning theory and technology, which is also conducive to promoting the further development of the DL-based PU technologies.

Thus, we proposed a PU method based on a spatial and channel attention network (SCAPU) to retrieve the true unwrapped phase from noisy interferograms with varying levels of noise. First, we construct a network suitable for unwrapping the wrapped phase images. This network utilizes Deeplabv3+ [29] as the backbone, adopts a serial-parallel atrous spatial pyramid pooling module (SPASPPM) [37], implements multi-scale skip connections between the encoder-decoder module, and fuses convolutional block attention module (CBAM) [38]. Here, the SPASPPM can obtain a larger receptive field while enhancing the correlation between feature maps with different convolution rates [39], the multi-scale skip connections promote fusion of the detailed phase information and fringe semantic information, and the CBAM can effectively extract semantic information in both the channel and spatial dimensions to improve the PU accuracy. Second, datasets with different noise levels are used to train the network using a previously proposed noise level evaluation system [31], and the trained network can effectively handle the PU for interferograms. Finally, the interferograms are unwrapped using the trained network with the same noise level as the interferograms.

II. PROPOSED METHOD

A. SCAPU NETWORK

The SCAPU network is shown in Fig. 1. As shown, the proposed network is based on the encoder-decoder module and utilizes Deeplabv3 + [27] as the backbone. The SCAPU network utilizes the SPASPPM, includes multi-scale skip connections between the encoder-decoder module, and fuses the CBAM (marked in the red dashed box in Fig.1).

1) *ENCODER

The encoder module comprises a DCNN and the SPASPPM. Here, the DCNN is the modified aligned Xception network [27], and its structure is shown in Fig. 2, including the input, middle and output flows. The image input to the DCNN refers to wrapped phase images with a resolution of 256 × 256. In the input layer of the DCNN, three low-level feature maps with the resolutions of 64 × 64, 32 × 32, and 16 × 16, are extracted. These low-level feature maps can

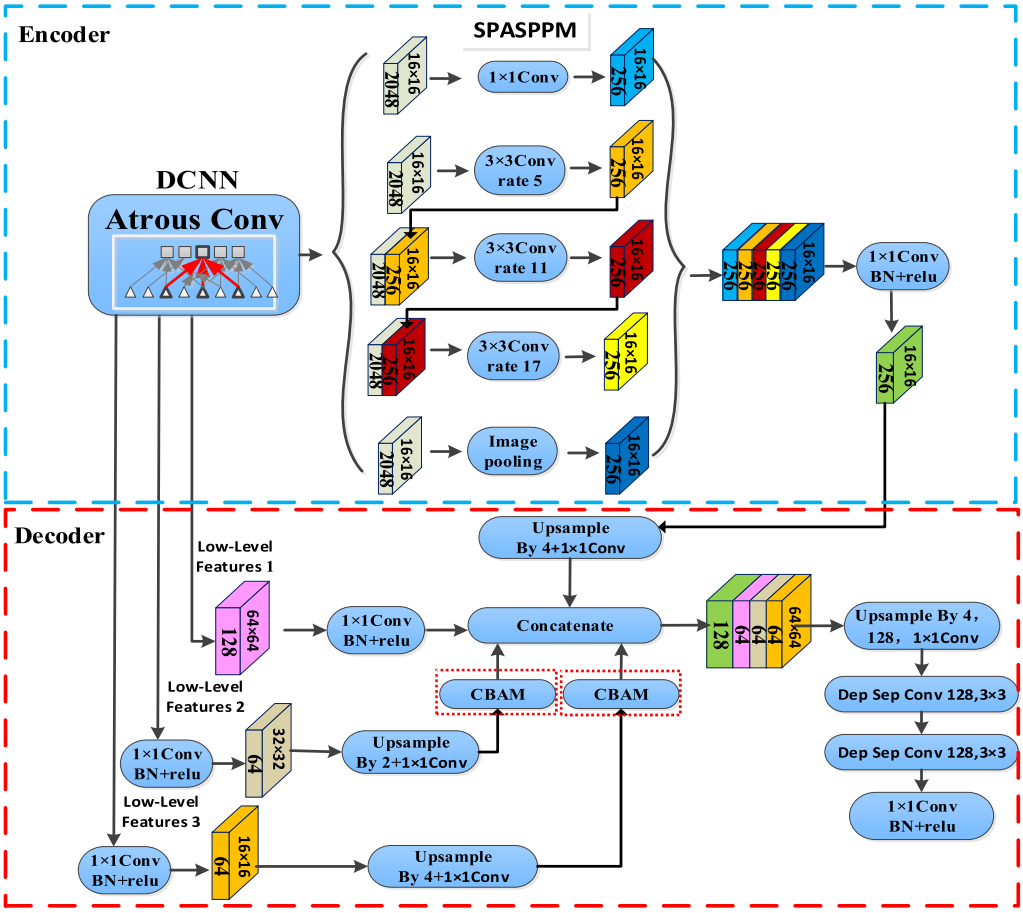

FIGURE 1. Architecture of the proposed SCAPU network.

provide abundant phase information for the feature maps output by the encoder module. The SPASPPM fuses feature maps with different scales, and utilizes a "1 × 1Convolution+BN (Batch-normalization) + RELU (Rectified Linear Unit)" operation to adjust the channel number of the output feature maps with a resolution of 16 × 16, with high semantic information (HSI).

2) *DECODER

In the decoder module, the channel number of three low-level feature maps with different scales, output by the DCNN, is adjusted by the "1 × 1Convolution+BN+RELU" operation, and the 64-channel feature maps with the resolutions of 64 × 64, 32 × 32, and 16 × 16 are obtained, respectively. Here, the feature maps with the resolutions of 32 × 32 and 16 × 16 are increased to a resolution of 64 × 64 by performing upsampling and a convolution operation, and then the CBAMs were separately applied to the two sets of feature maps whose resolution has been increased to 64 × 64. The fusion of multi-scale features and the application of CBAM facilitate the extraction of multi-scale feature information in the encoder module, thereby enhancing the representation ability of features. Especially, the multi-scale skip connections between the encoder-decoder module are used to promote fusion of the detailed phase information and semantic information from the feature maps with different resolutions. Then, three 64-channel feature maps with a resolution of 64 × 64 are obtained. These feature maps are referred to as the DCNN feature maps. In addition, the "Upsample by 4+1 × 1convolution" operation (i.e., a 4 × 4 bilinear interpolation upsampling convolution operation) is implemented on the HSI output by the encoder module. Subsequently, 128-channel feature maps with 64 × 64 resolution, are obtained and concatenated with the DCNN feature maps. After that, 128-channel feature maps with 256 × 256 resolution are obtained by performing a 4 × 4 bilinear interpolation upsampling convolution operation on the concatenated feature maps. Finally, two depth separable convolution layers and a "1 × 1 Convolution+BN+RELU" operation unit are employed to process the feature maps with a resolution of 256 × 256 to obtain the unwrapped phase of the wrapped phase image.

3) *SPASPPM

The SPASPPM [37] in Fig. 1 includes five branches, i.e., a 1 × 1 convolutional kernel, three 3 × 3 convolutional kernels with a sampling rate of each factor (5, 11, and 7), and

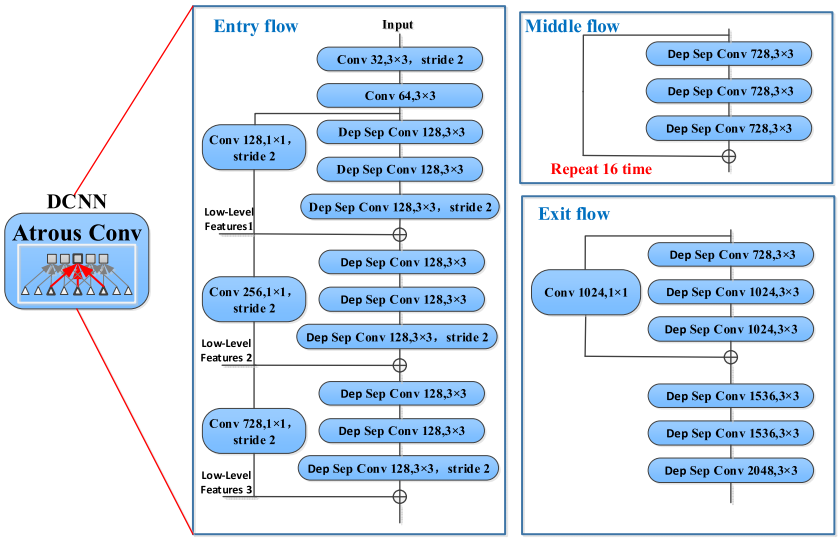

FIGURE 2. Schematic diagram of the Xception network.

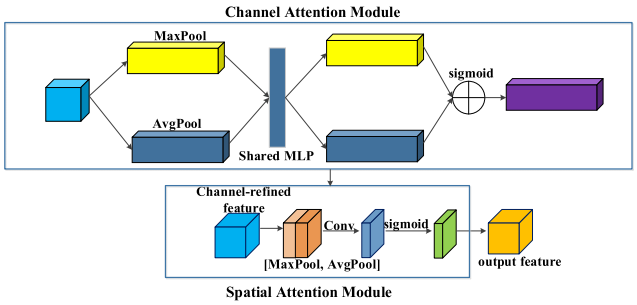

FIGURE 3. Schematic diagram of the CBAM.

an average pooling layer. Note that these five branches adopt a parallel structure. The branches of the 3 × 3 convolutional kernels adopt a serial connection method, and their inputs are composed of the high-level features generated by the DCNN and the output features of the former convolution models. Finally, the output features of each branch are fused to acquire the final feature map while enhancing the correlation between feature maps with different convolution rates. The SPASPPM can not only acquire a larger receptive field, but also enhance the correlation between feature maps with different convolution rates, which is conducive to capturing more multi-scale information and enhancing the ability of feature representation, thus avoiding the loss of phase information as much as possible while enhancing the ability to extract feature information from interferograms.

4) *CBAM

Fig. 3 shows the CBAM [38], which comprises a spatial attention module (SAM) and a channel attention module (CAM). Here, SAM and CAM aggregate phase information and dimension information by performing average pooling and maximum pooling operations on the spatial and channel axis, respectively. The CBAM can obtain the weight of each feature channel automatically by learning, and it can achieve good results by training the model such that the feature maps with more important information have higher weight, and those with less important information have lower weight. The CBAM can effectively extract the semantic information in both the channel and spatial dimensions, which is conducive to acquire more valuable feature representation from feature maps for improving the PU accuracy while the network parameters are not significantly increased. More details about the CBAM can be found in [38].

B. NETWORK DATASET

Implementation of the proposed SCAPU network is divided into training and prediction stages, as shown in Fig. 4, where Fig. 4(a) shows the training for the networks and Fig. 4(b) shows PU for the interferograms employing the trained networks.

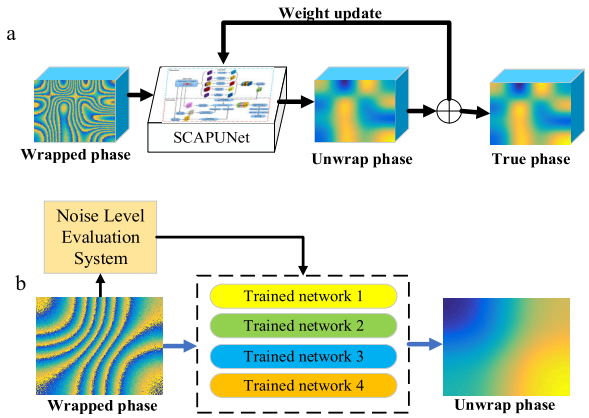

FIGURE 4. Schematic diagram of the SCAPU process: (a) training the SCAPU network; (b) PU for interferograms using the trained networks.

In this study, four groups of training sets with different levels of noise were constructed and used to train the network suitable for unwrapping interferograms with different

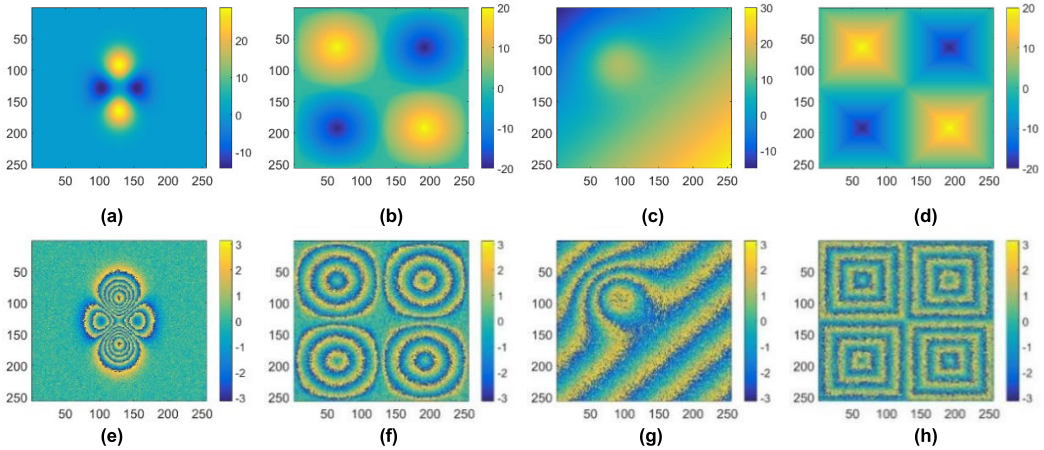

FIGURE 5. Simulated interferograms: (a–d) represented the true phases of mountainous terrain, four cones, simulated mountains, and four pyramids, (e–h) represented the corresponding wrapped phases in (a) –(d).

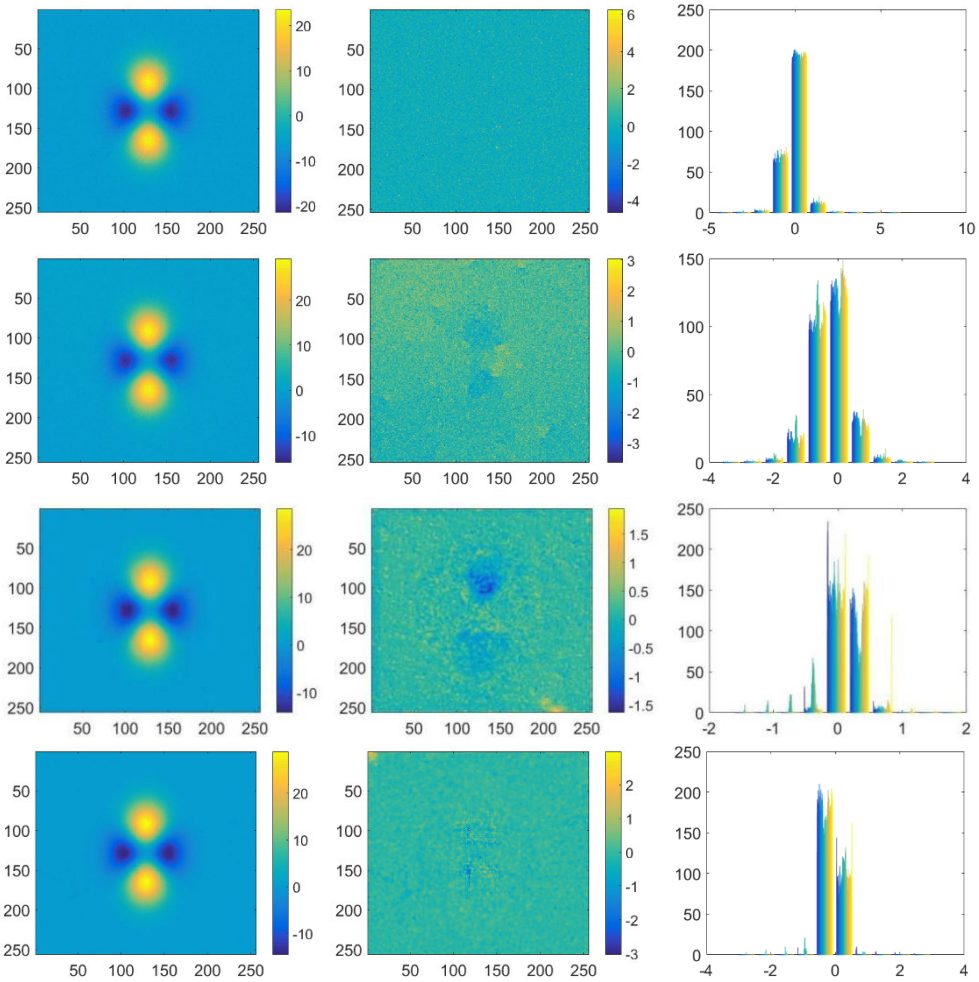

FIGURE 6. Results acquired by applying the different PU method to unwrap Fig. 5(e). From-left-to-right, each column represented the unwrapped phase, the PUE, and the PUE histogram, respectively; From-top-to-bottom, each row represented the solutions for the QGPU, ILS, UNETPU and SCAPU methods, respectively.

noise levels, consequently, four trained networks including the trained network1, trained network2, trained network3, and trained network4, suitable for different noise levels of the interferograms, were achieved, as shown in Fig. 4(b). Note that detailed information about the noise level evaluation approach of the interferograms, and the approaches

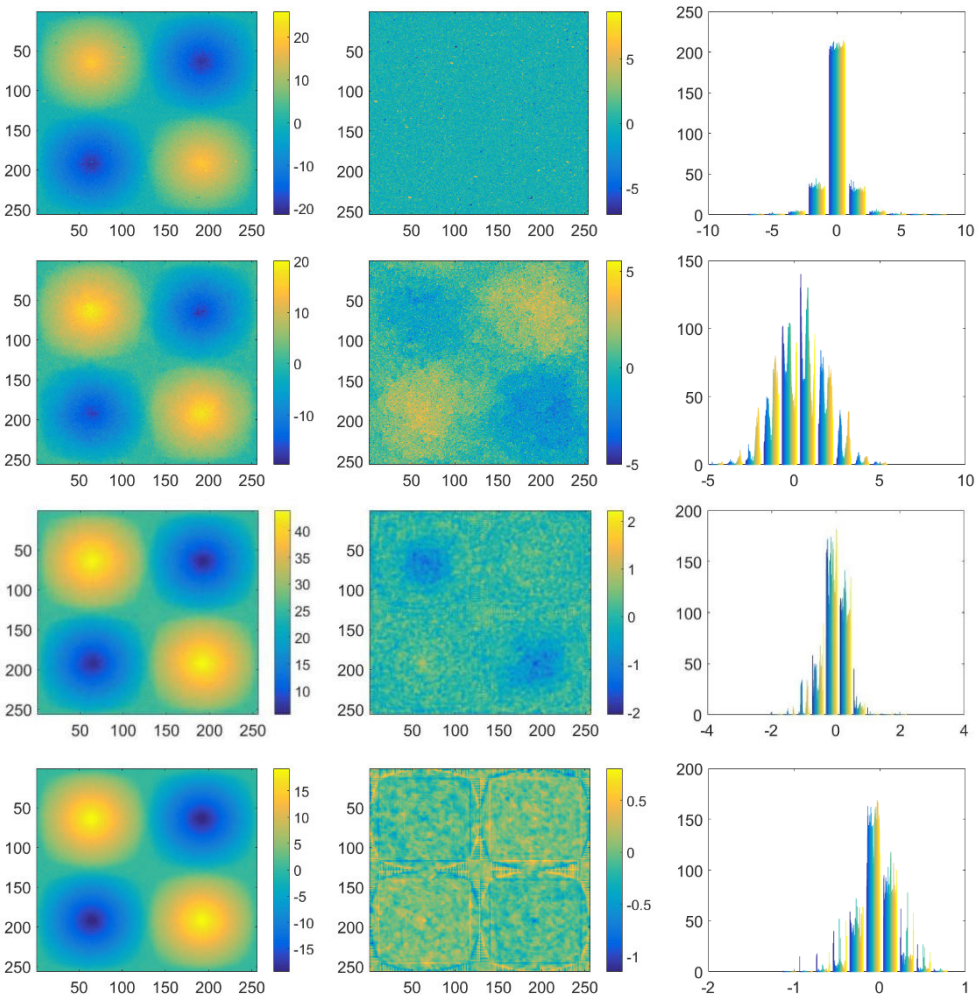

FIGURE 7. Results acquired by applying the different PU method to unwrap Fig. 5(f). From-left-to-right, each column represented the unwrapped phase, the PUE, and the PUE histogram, respectively; From-top-to-bottom, each row represented the solutions for the QGPU, ILS, UNETPU and SCAPU methods, respectively.

of constructing datasets and training network were reported in [31].

The dataset of each group with different noise levels contains 31,000 sets of data, which were generated in the following three ways: (1) The dataset of 3000 sets was constructed referring to the dataset generation method in the literature [27]. (2) The dataset of 4000 sets was constructed referring to the dataset generation method in the literature [30]. (3) The dataset of 24,000 sets of InSAR phase data [31] was generated by converting the digital elevation maps of Datong City, Shanxi Province, Huangshan City, Anhui Province, and Jinhua City, Zhejiang Province in China into the phase. The image size in this dataset is 256 × 256, and the phase range of the label image was defined in 0–60 radians. The network was trained based on the Keras2.4.3 DL framework. In addition, the network was trained using a personal computer with an Inter Xeon W-2245 3.9GHz CPU, 128GB RAM, and an NVIDIA GeForce RTX 3080 graphics processing unit. The network was trained with the adaptive moment estimation optimizer (i.e., the Adam optimizer) and the mean square error (MSE) loss function. Here, the initial learning rate was 0.001, the number of training epochs was set to 200, the minimum training batch was eight, and the time for the trained model to reach convergence was about approximately 60 hours.

III. EXPERIMENT AND ANALYSIS

A. SIMULATED DATA EXPERIMENTS

To show the performance of the SCAPU network, we compared to the quality-guided PU (QGPU) method [9], the iterative least squares (ILS) method [14] and the representative UNETPU [30] method by unwrapping the four different types of simulated interferograms shown in Fig. 5. Here, Figs. 5(a)–5(d) showed the true phases of the mountainous terrain, four cones, simulated mountains and four pyramids with a resolution of 256 × 256, respectively. The wrapped phases corresponding to the true phases of Figs. 5(a)–5(d), were shown in Figs. 5(e)–5(h), whose SNR values were

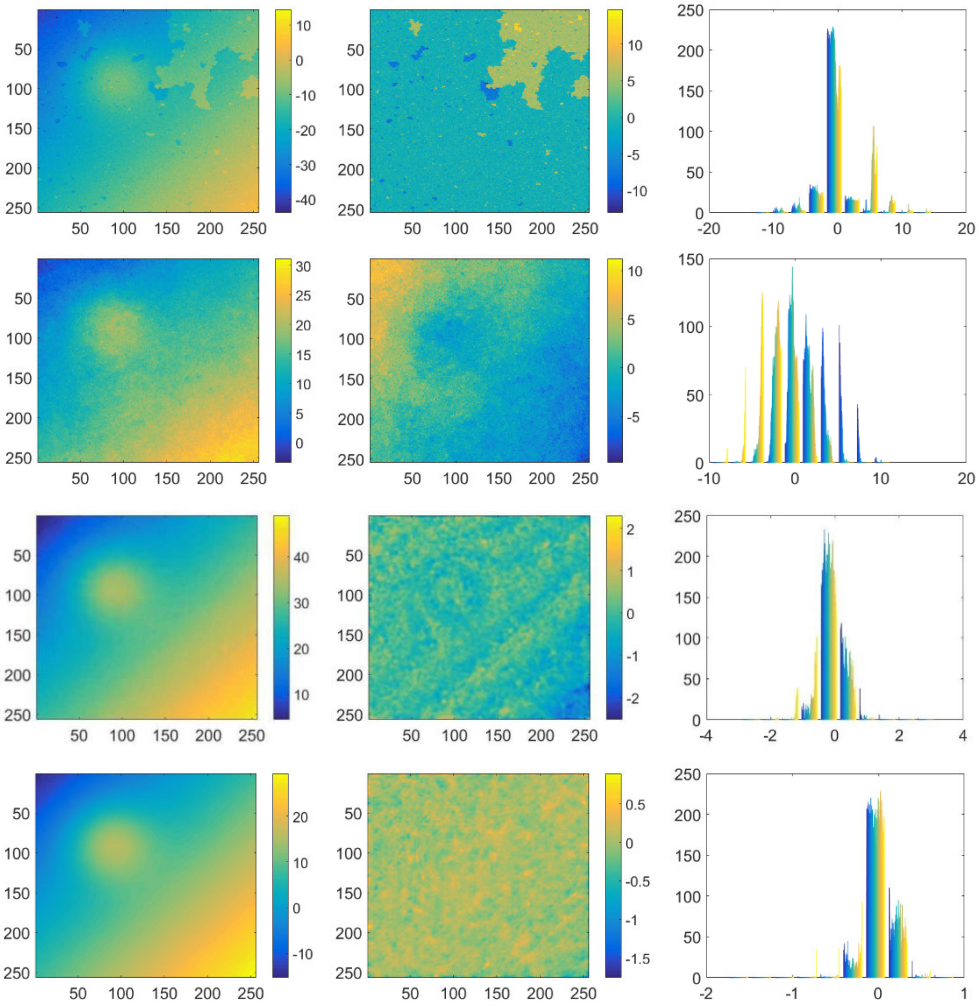

FIGURE 8. Results acquired by applying the different PU method to unwrap Fig. 5(g). From-left-to-right, each column represented the unwrapped phase, the PUE, and the PUE histogram, respectively; From-top-to-bottom, each row represented the solutions for the QGPU, ILS, UNETPU and SCAPU methods, respectively.

4.94 dB, 1.42 dB, -1.07 dB and -1.07 dB, respectively, and the corresponding noise levels [31] were 1, 2, 3 and 3, respectively.

The unwrapped results for the wrapped phases in Figs. 5(e)–5(h) acquired by applying the QGPU, ILS, UNETPU and SCAPU methods were shown in Figs. 6–9, respectively. Here, each column in Figs. 6–9 showed the unwrapped phase, the PU errors (PUE) and the corresponding the PUE histogram (i.e., the histogram of the PUE) delivered by the above four methods, respectively. Due to the high SNR of the interferograms shown in Figs. 5(e) -5(f), both the QGPU and ILS methods achieved good unwrapped results from these interferograms, as shown in the first two rows of Figs. 6-7, respectively, where the dynamic range of the PUE delivered by the QGPU method are small, and its errors are mainly distributed in the interval of [6, -5] and [7, -6], respectively, while the dynamic range of the PUE delivered by the ILS method are also small, and its errors are mainly distributed in the interval of [3, -4] and [5, -5], respectively. In the case of low SNR of interferograms (such as Figs. 5(g) –5(h)), the errors caused by the QGPU method spread among the entire image in the unwrapping process, which resulted in very inconsistent unwrapped phases and large errors, as shown in the first row of Figs. 8-9. The unwrapped phases acquired by applying the ILS method to unwrap Figs. 5(g)–5(h), were roughly continuous, however, like the QGPU method, the errors delivered by this method were also large, as shown in the second row of Figs. 8-9. The solutions delivered by the UNETPU and SCAPU methods were showed in the third and fourth rows of Figs. 6-9, as can be seen from Figs. 8-9 that compared to the ILS and QGPU methods, these two methods obtained better unwrapped results and the phase errors were smaller, even when the interferograms were severely noisy. The-root-means-square errors (RMSE) of these methods for unwrapping the interferograms with different SNR values were reported in TABLE 1. Here, the RMSE values represent the median value of the errors computed over 30 simulation runs. The average

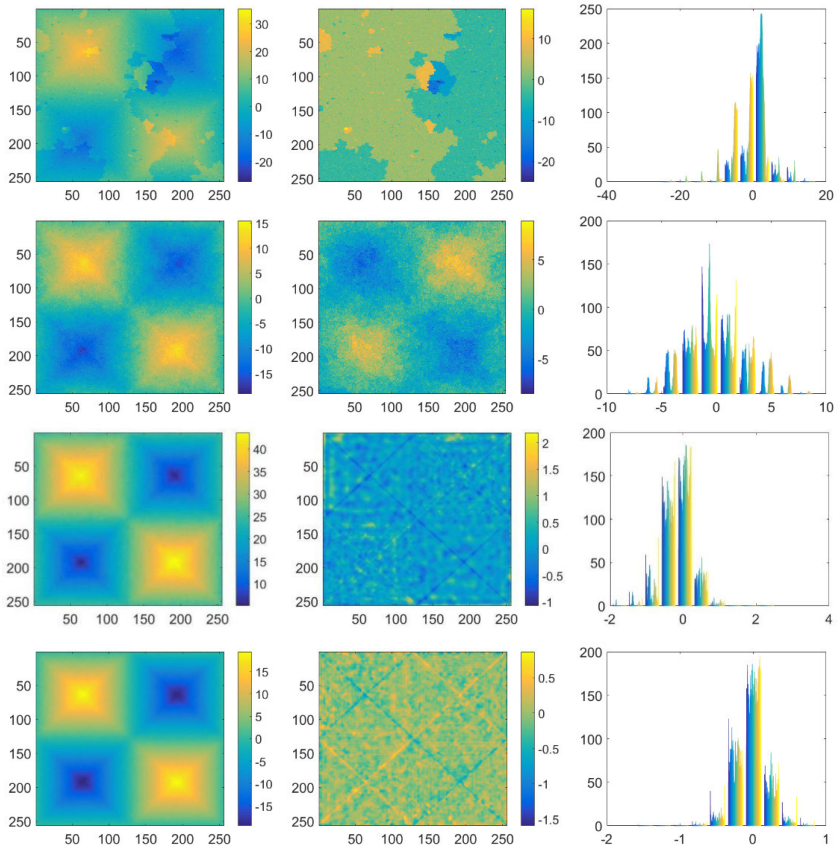

FIGURE 9. Results acquired by applying the different PU method to unwrap Fig. 5(h). From-left-to-right, each column represented the unwrapped phase, the PUE, and the PUE histogram, respectively; From-top-to-bottom, each row represented the solutions for the QGPU, ILS, UNETPU and SCAPU methods, respectively.

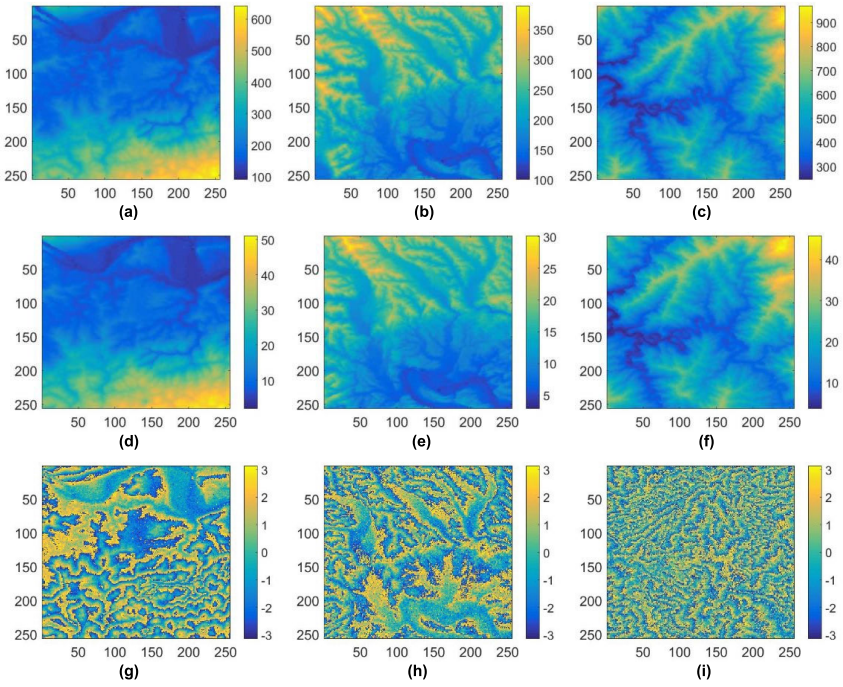

FIGURE 10. Synthetic interferograms derived from DEM: (a–c) represented respectively the DEMs of three regions in Hunan, in China, (d–f) represented respectively the true unwrapped phases corresponding to (a) –(c), (g–i) represented respectively noisy wrapped phases corresponding to (d)–(f).

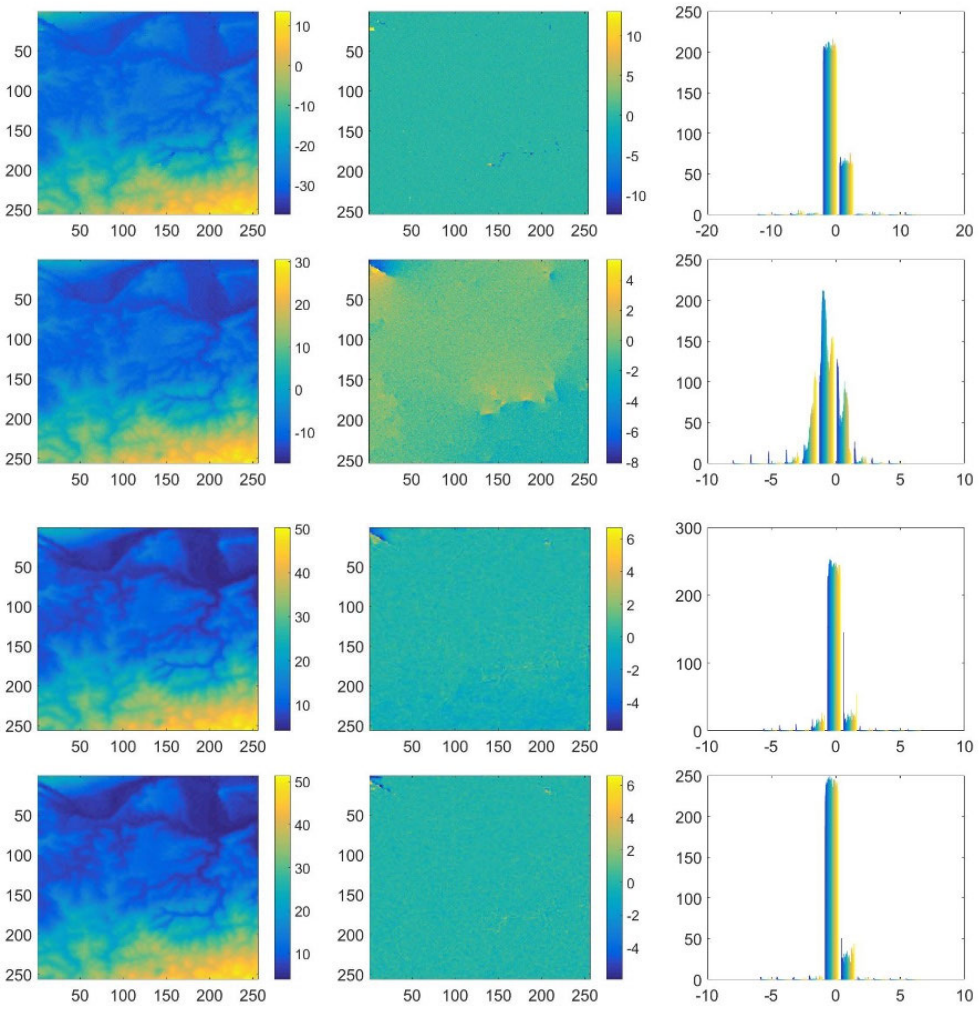

FIGURE 11. Results acquired by applying the different PU method to unwrap Fig. 10(g) . From-left-to-right, each column represented the unwrapped phase, the rewrapped phase, the PUE, and the PUE histogram, respectively; From-top-to-bottom, each row represented the solutions for the QGPU, ILS, UNETPU and SCAPU methods, respectively.

TABLE 1. Comparison of the RMSE values under different noise levels.

Image	SNR	Noise Level	QGPU	ILS	UNETPU	SCAPU
mountainous terrain	4.94dB	1	0.4624	0.5431	0.2308	0.1821
	1.42dB	2	0.8670	1.3020	0.2126	0.1879
	-1.07dB	3	3.5028	1.9835	0.6725	0.2013
four cones	4.94dB	1	0.4601	0.5489	0.3651	0.1444
	1.42dB	2	0.8023	1.3939	0.3058	0.1664
	-1.07dB	3	3.1824	2.5424	0.3664	0.1829
simulated mountains	4.94dB	1	0.4591	0.7346	0.4689	0.1168
	1.42dB	2	0.7994	1.6452	0.3446	0.1186
	-1.07dB	3	2.6973	2.9908	0.3423	0.1248
four pyramids	4.94dB	1	0.4604	0.5576	0.3185	0.1324
	1.42dB	2	0.8043	1.3935	0.3341	0.1486
	-1.07dB	3	3.9806	2.4443	0.3322	0.1693

times required to unwrap the interferograms shown in Figs. 5(e)–5(h) using the PU methods were shown in TABLE 2. As can be further seen from TABLE 1 that the SCAPU method not only provided better accuracy than the QGPU and ILS methods, but also the errors delivered by this method were obviously less than those of the UNETPU method. Note that the time costs of the SCAPU and UNETPU method were less than those of the other two methods.

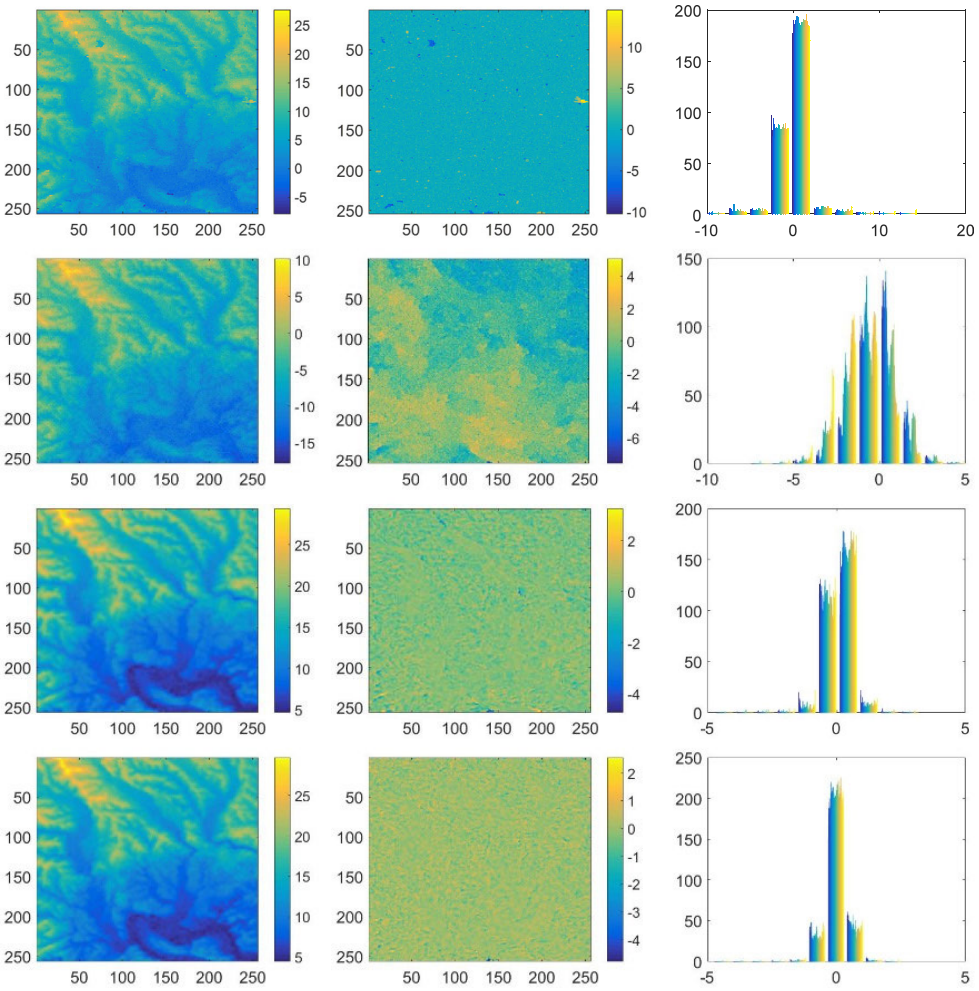

FIGURE 12. Results acquired by applying the different PU method to unwrap Fig. 10(h) . From-left-to-right, each column represented the unwrapped phase, the rewrapped phase, the PUE, and the PUE histogram, respectively; From-top-to-bottom, each row represented the solutions for the QGPU, ILS, UNETPU and SCAPU methods, respectively.

TABLE 2. Runtime time of the PU methods (s).

QGPU	ILS	UNETPU	SCAPU
28.9695	0.8987	0.0512	0.0912

TABLE 3. SRTM parameter.

β	R	λ	θ	α
60m	231Km	0.056	45°	45°

In summary, the proposed SCAPU method demonstrated strong robustness compared to the QGPU, ILS and UNETPU methods, and obvious efficiency advantages compared to the QGPU and ILS methods. Here, the QGPU and ILS methods were worked with MATLAB R2016b, and the SCAPU and UNETPU methods were performed on Python 3.8.

B. SYNTHETIC DATA EXPERIMENTS OVER SRTM DEM

Figs. 10(a)-10(c) showed respectively the digital elevation maps (DEMs) of three regions in Hunan, in China, derived from the SRTM DEM, and were marked as SRTM-DEM1, SRTM-DEM2, SRTM-DEM3, respectively (to for the convenience of subsequent description). Figs. 10(d)-10(f) denoted true unwrapped phases corresponding to three DEMs shown in Figs. 10(a)-10(c), generated according to the SRTM parameters listed in Table. 3. Figs. 10(g)-10(i) denoted noisy wrapped phase images corresponding to the true phases shown in Figs. 10(d)-10(f), whose SNR values were 4.94 dB, 1.42 dB and -1.07 dB, respectively, and the corresponding noise levels were 1, 2 and 3, respectively.

To further show the performance of the SCAPU network, the QGPU, ILS, UNETPU and SCAPU methods were used to the wrapped phases shown in Figs. 10(g)–10(i).

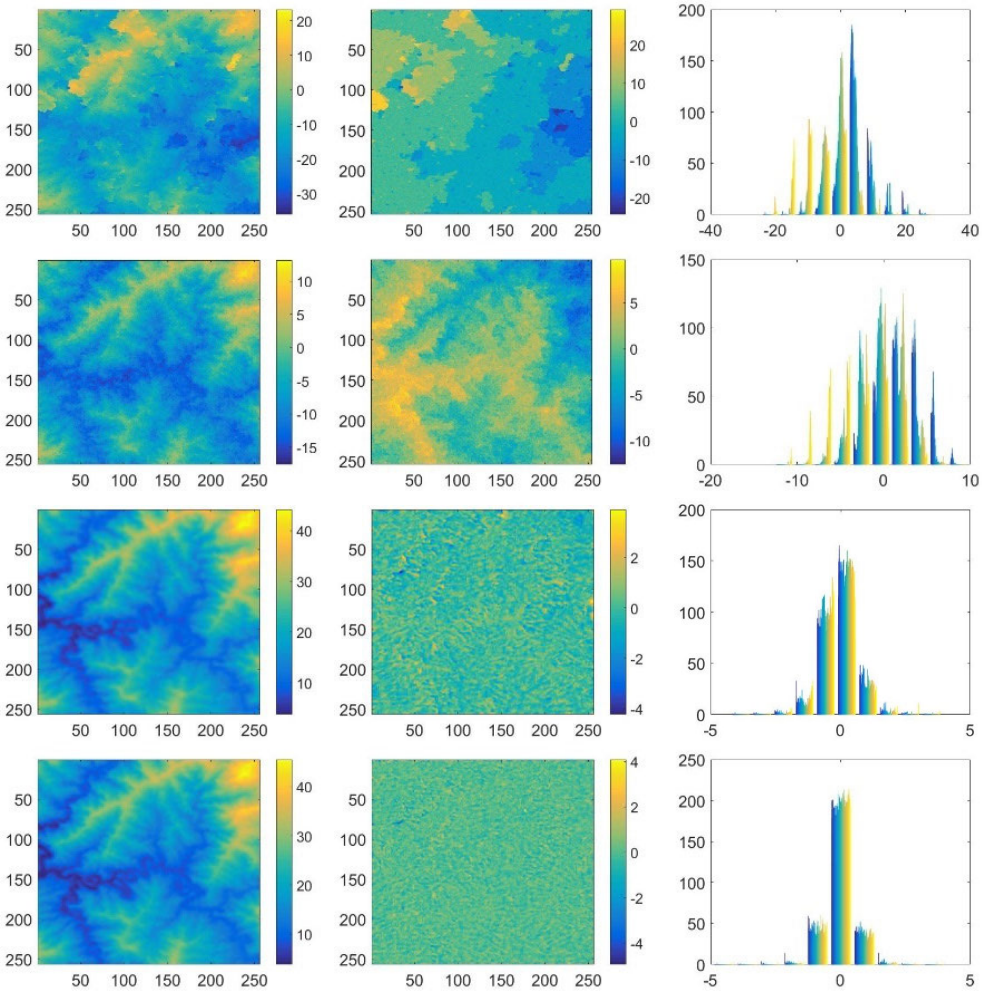

FIGURE 13. Results acquired by applying the different PU method to unwrap Fig. 10(i) . From-left-to-right, each column represented the unwrapped phase, the rewrapped phase, the PUE, and the PUE histogram, respectively; From-top-to-bottom, each row represented the solutions for the QGPU, ILS, UNETPU and SCAPU methods, respectively.

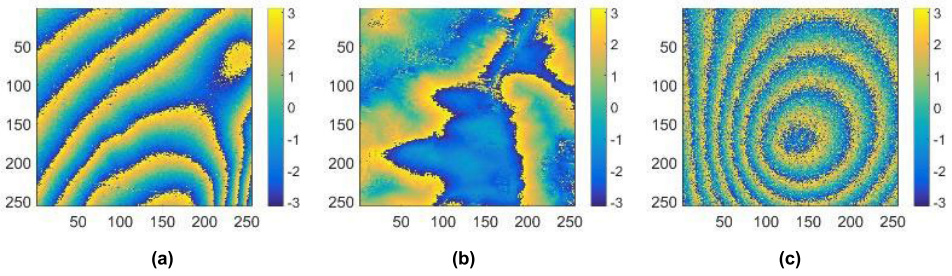

FIGURE 14. Measured interferograms: (a) part of interferogram over Bam, Iran; (b) part of interferogram over Yunnan, and (c) Rahul interferogram

Figs. 11-13 showed the unwrapped results acquired by these method.

Each column in Figs. 11–13 showed the unwrapped phase, the PUE and the corresponding PUE histogram delivered by different methods, respectively. In addition, the RMSE of these methods for unwrapping the interferograms with different SNR values were reported in TABLE 4. From Figs. 11-13 and TABLE 4, the following can be seen: (1) the dynamic range of the PUE delivered by the UNETPU and SCAPU methods was far less than that of the QGPU method in all cases; (2) not only was the dynamic range of the PUE delivered by the UNETPU and SCAPU method less than that

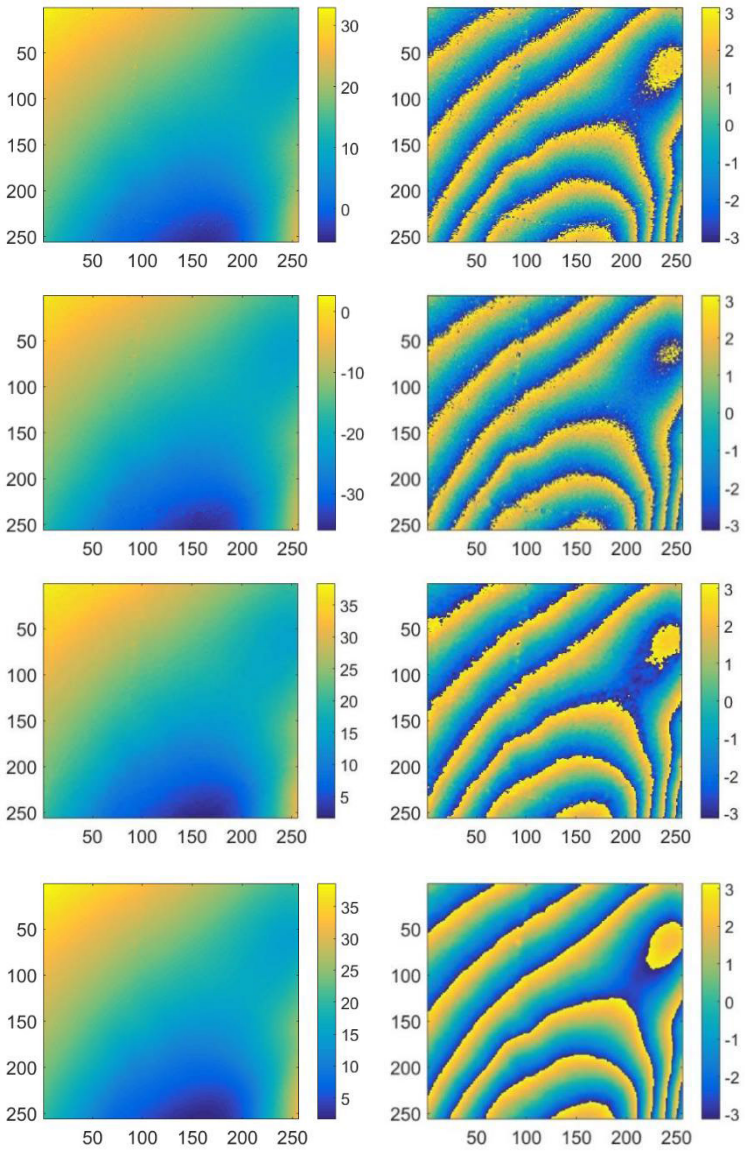

FIGURE 15. Results acquired by applying the different PU method to unwrap Fig. 14(a) . The left and right columns represented the unwrapped and rewrapped phases, respectively; From-top-to-bottom, each row represented the solutions for the QGPU, ILS, UNETPU and SCAPU methods, respectively.

of the ILS method in all cases, but also compared with the ILS method, most of the errors delivered by these two methods were distributed around 0, therefore, it can be expected that the RMSE of these two methods is much smaller than that of the ILS method; (3) the errors delivered by the SCAPU method were not only less than those of the QGPU and ILS methods, but also less than those of the UNETPU method in all cases.

C. MEASURED DATA EXPERIMENTS

Fig. 14 showed the measured interferograms used to further test the performance of the SCAPU method. Fig. 14(a) denoted the wrapped phase image derived from an interferogram over Bam, Iran [31], Fig. 14(b) denoted the wrapped phase image from an interferogram over Yunnan, Yangbi County, Yunnan Province, China (acquired by the Sentinel-1A satellite at 21:48 on May 21, 2021), and Fig. 14(c) denoted the Rahul interferogram [40].

The noise levels of the interferograms shown Figs. 14(a)–14(c), were 1, 2, 3, respectively. The unwrapped results acquired by applying the QGPU, ILS, UNETPU and proposed SCAPU methods were shown in Figs. 15–17, respectively, where the left columns of Figs. 15–17 and their corresponding right columns showed the unwrapped phases and the corresponding rewrapped phases acquired by applying the compared methods, respectively. As shown in

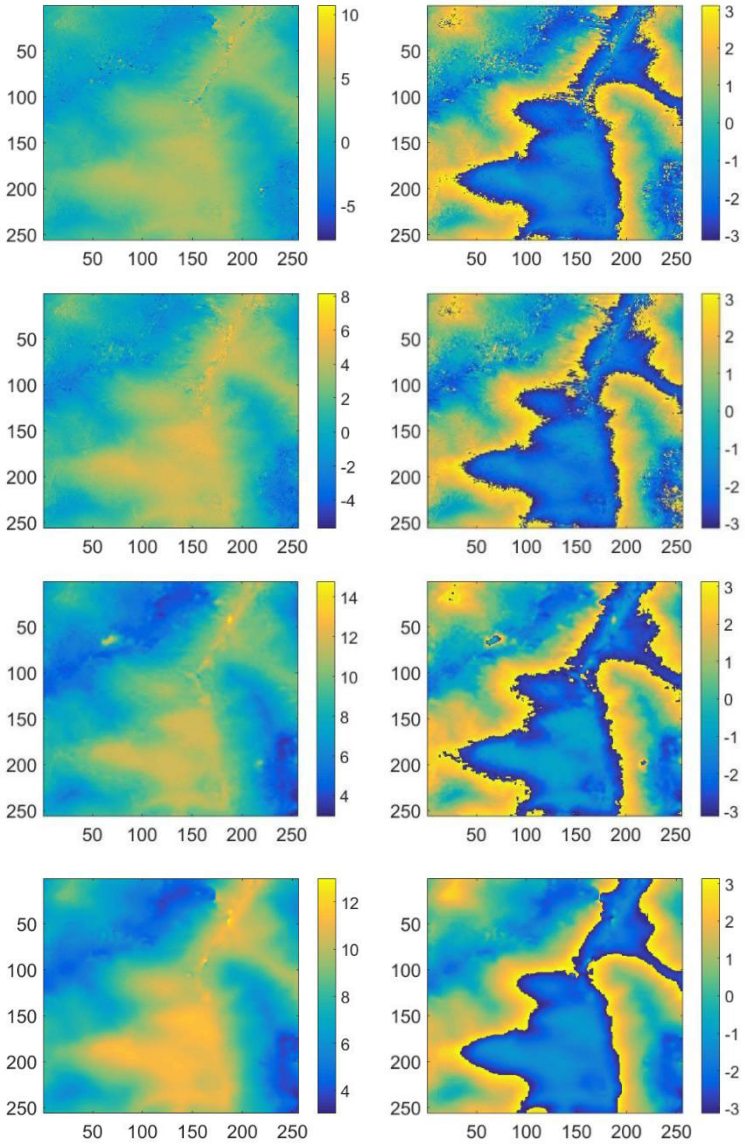

FIGURE 16. Results acquired by applying the different PU method to unwrap Fig. 14(b) . The left and right columns represented the unwrapped and rewrapped phases, respectively; From-top-to-bottom, each row represented the solutions for the QGPU, ILS, UNETPU and SCAPU methods, respectively.

TABLE 4. Comparison of the RMSE values under different noise levels.

Image	SNR	Noise Level	QGPU	ILS	UNETPU	SCAPU
SRTM DEM1	4.94dB	1	0.6143	1.1113	0.4051	0.3190
	1.42dB	2	1.2390	2.2424	0.5459	0.3691
	-1.07dB	3	5.1747	3.8801	0.6376	0.4311
SRTM DEM 2	4.94dB	1	0.5115	1.0811	0.3305	0.2887
	1.42dB	2	1.3465	1.4235	0.3996	0.3351
	-1.07dB	3	4.8882	2.0658	0.5126	0.3931
SRTM DEM 3	4.94dB	1	0.5874	1.2007	0.3900	0.3377
	1.42dB	2	1.5679	1.9996	0.4372	0.3802
	-1.07dB	3	6.8666	3.2515	0.5660	0.4366

the left column of Fig. 17, a lot of phase inconsistencies appeared in the unwrapped phase acquired by applying the QGPU method for the Rahul interferogram. In addition, the unwrapped phases acquired by applying the ILS method in

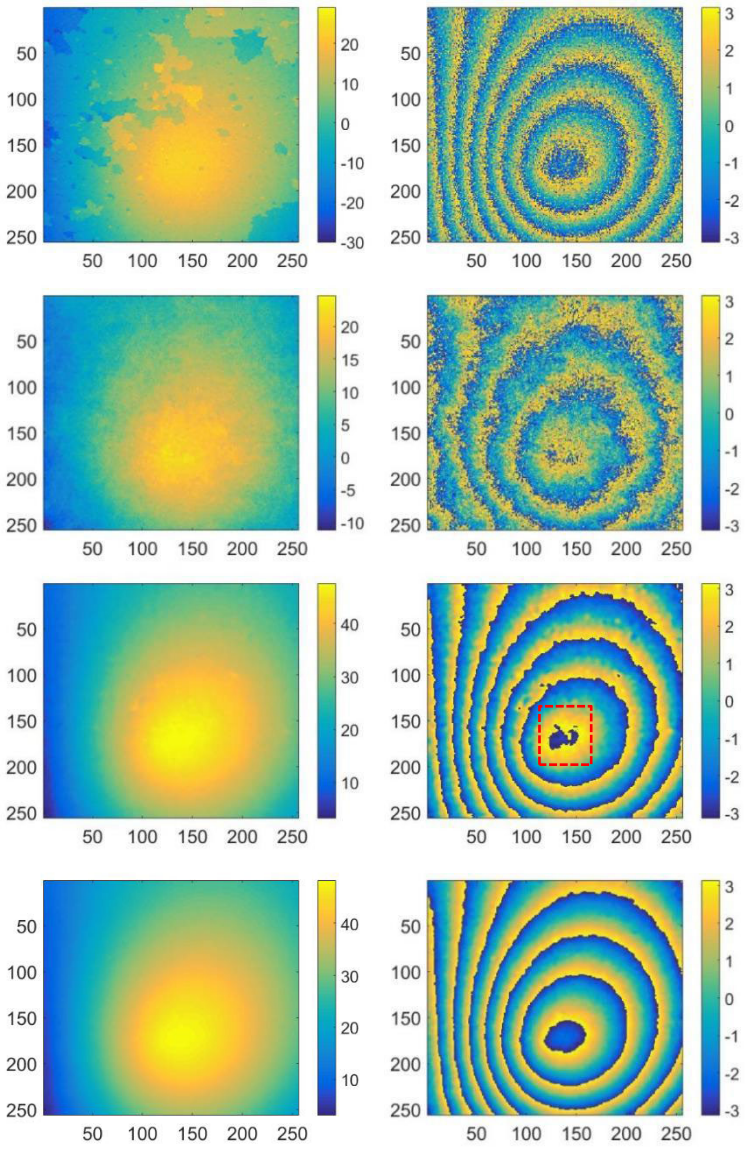

FIGURE 17. Results acquired by applying the different PU method to unwrap Fig. 14(c) . The left and right columns represented the unwrapped and rewrapped phases, respectively; From-top-to-bottom, each row represented the solutions for the QGPU, ILS, UNETPU and SCAPU methods, respectively.

the left columns of Figs. 15-17 were relatively continuous; however, clearly inconsistent fringe with the measured interferogram shown in Fig. 14(c), appeared in the rewrapped phase in the right column of the second row of Fig. 17, which indicated that the unwrapped results of Fig. 14(c) acquired by applying this method were unreliable. The unwrapped results acquired by applying the UNETPU and proposed SCAPU methods were shown in the third and fourth rows in Figs. 15–17, respectively, where the left columns of the third and fourth rows of Figs. 15–17 and their corresponding right columns showed the unwrapped phases and the corresponding rewrapped phases acquired by applying these two methods, respectively. As shown in the left column of the third row of Figs. 15-17, like the ILS method, the unwrapped phases delivered by the UNETPU method is roughly continuous; however, it can also be seen from the right column of the third row of Fig. 17 that the fringes of the UNETPU rewrapped phases marked in the red dashed box are clearly inconsistent with those of the measured interferogram shown in Fig. 14(c), which showed that the unwrapped phases corresponding to the marked area of the rewrapped phases, delivered by this method may not be reliable. Compared to QGPU, ILS UNETPU methods, the unwrapped phases acquired by applying the SCAPU method were continuously smooth, and the rewrapped phases were consistent with the interferograms shown in Figs. 14(a)–14(c), while with very less residual noise. These results demonstrated that the SCAPU method can effectively suppress phase noise

and obtain better unwrapped results from noisy measured interferograms.

IV. CONCLUSION

In this paper, we have proposed the SCAPU method to carry out PU operations on wrapped phase images using a DL network to construct a mapping relationship between the wrapped phase and its corresponding unwrapped phase, and the trained network was used to unwrap the interferograms with different noise levels. The SCAPU method was evaluated experimentally, and the experimental data obtained on both simulated and measured interferograms showed that the SCAPU method was effective in PU for interferograms. Compared to two traditional methods (i.e., the QGPU and ILS methods) and the UNETPU method, the proposed SCAPU method obtained more robust results, however with lower time costs than the QGPU and ILS methods.

REFERENCES

[1] H. Yu, Y. Lan, H. Lee, and N. Cao, "2-D phase unwrapping using minimum infinity-norm," *IEEE Geosci. Remote Sens. Lett.*, vol. 15, no. 12, pp. 1887–1891, Dec. 2018.

[2] H. Yu, Y. Lan, J. Xu, D. An, and H. Lee, "Large-scale L^0-norm and L^1-norm 2-D phase unwrapping," *IEEE Trans. Geosci. Remote Sens.*, vol. 55, no. 8, pp. 4712–4728, Aug. 2017.

[3] Z. Yuan, Z. Lu, L. Chen, and X. Xing, "A closed-form robust cluster-analysis-based multibaseline InSAR phase unwrapping and filtering algorithm with optimal baseline combination analysis," *IEEE Trans. Geosci. Remote Sens.*, vol. 58, no. 6, pp. 4251–4262, Jun. 2020.

[4] L. Zhou, H. Yu, Y. Lan, S. Gong, and M. Xing, "CANet: An unsupervised deep convolutional neural network for efficient cluster-analysis-based multibaseline InSAR phase unwrapping," *IEEE Trans. Geosci. Remote Sens.*, vol. 60, 2022, Art. no. 5212315.

[5] H. Yu, Y. Lan, Z. Yuan, J. Xu, and H. Lee, "Phase unwrapping in InSAR : A review," *IEEE Geosci. Remote Sens. Mag.*, vol. 7, no. 1, pp. 40–58, Mar. 2019.

[6] D. C. Ghiglia and D. P. Mark, *Two-Dimensional Phase Unwrapping: Theory, Algorithms, and Software*, vol. 4. New York, NY, USA: Wiley, 1998.

[7] B. Osmanoğlu, F. Sunar, S. Wdowinski, and E. Cabral-Cano, "Time series analysis of InSAR data: Methods and trends," *ISPRS J. Photogramm. Remote Sens.*, vol. 115, pp. 90–102, May 2016.

[8] C. Li and D.-Y. Zhu, "A residue-pairing algorithm for InSAR phase unwrapping progress," *Prog. Electromagn. Res.*, vol. 95, pp. 341–354, 2009.

[9] M. Zhao, L. Huang, Q. Zhang, X. Su, A. Asundi, and Q. Kemao, "Quality-guided phase unwrapping technique: Comparison of quality maps and guiding strategies," *Appl. Opt.*, vol. 50, no. 33, pp. 6214–6224, 2011.

[10] R. M. Goldstein, H. A. Zebker, and C. L. Werner, "Satellite radar interferometry: Two-dimensional phase unwrapping," *Radio Sci.*, vol. 23, no. 4, pp. 713–720, Jul. 1988.

[11] M. Costantini, "A novel phase unwrapping method based on network programming," *IEEE Trans. Geosci. Remote Sens.*, vol. 36, no. 3, pp. 813–821, May 1998.

[12] J. Ting-chen, "Ameliorative minimum cost flow algorithm for phase unwrapping," *Proc. Environ. Sci.*, vol. 10, pp. 2560–2566, Jan. 2011.

[13] C. W. Chen and H. A. Zebker, "Network approaches to two-dimensional phase unwrapping: Intractability and two new algorithms," *J. Opt. Soc. Amer. A, Opt. Image Sci.*, vol. 17, no. 3, pp. 401–414, Mar. 2000.

[14] D. C. Ghiglia and L. A. Romero, "Robust two-dimensional weighted and unweighted phase unwrapping that uses fast transforms and iterative methods," *J. Opt. Soc. Amer. A, Opt. Image Sci.*, vol. 11, no. 1, pp. 107–117, 1994.

[15] G. H. Kaufmann, G. E. Galizzi, and P. D. Ruiz, "Evaluation of a preconditioned conjugate-gradient algorithm for weighted least-squares unwrapping of digital speckle-pattern interferometry phase maps," *Appl. Opt.*, vol. 37, no. 14, pp. 3076–3084, 1998.

[16] M. D. Pritt and J. S. Shipman, "Least-squares two-dimensional phase unwrapping using FFT's," *IEEE Trans. Geosci. Remote Sens.*, vol. 32, no. 3, pp. 706–708, May 1994.

[17] M. D. Pritt, "Phase unwrapping by means of multigrid techniques for interferometric SAR," *IEEE Trans. Geosci. Remote Sens.*, vol. 34, no. 3, pp. 728–738, May 1996.

[18] D. C. Ghiglia and L. A. Romero, "Minimum L^p-norm two-dimensional phase unwrapping," *J. Opt. Soc. Amer. A, Opt. Image Sci.*, vol. 13, no. 10, pp. 1999–2013, Oct. 1996.

[19] X. Xie and Y. Lee, "Enhanced phase unwrapping algorithm based on unscented Kalman filter, enhanced phase gradient estimator, and path-following strategy," *Appl. Opt.*, vol. 53, no. 18, pp. 4049–4060, 2014.

[20] X. Xie, "Iterated unscented Kalman filter for phase unwrapping of interferometric fringes," *Opt. Exp.*, vol. 24, no. 17, pp. 18872–18897, 2016.

[21] X. Xianming and P. Yiming, "Multi-baseline phase unwrapping algorithm based on the unscented Kalman filter," *IET Radar, Sonar Navigat.*, vol. 5, no. 3, pp. 296–304, 2011.

[22] J. J. Martinez-Espla, T. Martinez-Marin, and J. M. Lopez-Sanchez, "A particle filter approach for InSAR phase filtering and unwrapping," *IEEE Trans. Geosci. Remote Sens.*, vol. 47, no. 4, pp. 1197–1211, Apr. 2009.

[23] X. M. Xie, Y. M. Pi, and B. Peng, "Phase unwrapping: An unscented particle filtering approach," *Acta Electronica Sinica*, vol. 39, no. 3, pp. 705–709, 2011.

[24] X. Xie and G. Dai, "Unscented information filtering phase unwrapping algorithm for interferometric fringe patterns," *Appl. Opt.*, vol. 56, no. 34, pp. 9423–9434, Dec. 2017.

[25] G. E. Spoorthi, S. Gorthi, and R. K. S. S. Gorthi, "PhaseNet: A deep convolutional neural network for two-dimensional phase unwrapping," *IEEE Signal Process. Lett.*, vol. 26, no. 1, pp. 54–58, Jan. 2019.

[26] J. Zhang, X. Tian, J. Shao, H. Luo, and R. Liang, "Phase unwrapping in optical metrology via denoised and convolutional segmentation networks," *Opt. Exp.*, vol. 27, no. 10, pp. 14903–14912, 2019.

[27] T. Zhang, S. Jiang, Z. Zhao, K. Dixit, X. Zhou, J. Hou, Y. Zhang, and C. Yan, "Rapid and robust two-dimensional phase unwrapping via deep learning," *Opt. Exp.*, vol. 27, no. 16, pp. 23173–23185, 2019.

[28] G. E. Spoorthi, R. K. S. S. Gorthi, and S. Gorthi, "PhaseNet 2.0: Phase unwrapping of noisy data based on deep learning approach," *IEEE Trans. Image Process.*, vol. 29, pp. 4862–4872, 2020.

[29] F. Sica, F. Calvanese, G. Scarpa, and P. Rizzoli, "A CNN-based coherence-driven approach for InSAR phase unwrapping," *IEEE Geosci. Remote Sens. Lett.*, vol. 19, pp. 1–5, 2022.

[30] K. Wang, Y. Li, Q. Kemao, J. Di, and J. Zhao, "One-step robust deep learning phase unwrapping," *Opt. Exp.*, vol. 27, no. 10, pp. 15100–15115, 2019.

[31] X. Xie, X. Tian, Z. Shou, Q. Zeng, G. Wang, Q. Huang, M. Qin, and X. Gao, "Deep learning phase-unwrapping method based on adaptive noise evaluation," *Appl. Opt.*, vol. 61, no. 23, pp. 6861–6870, 2022.

[32] L. Zhou, H. Yu, V. Pascazio, and M. Xing, "PU-GAN: A one-step 2-D InSAR phase unwrapping based on conditional generative adversarial network," *IEEE Trans. Geosci. Remote Sens.*, vol. 60, 2022, Art. no. 5221510.

[33] L. Zhou, H. Yu, Y. Lan, and M. Xing, "Deep learning-based branch-cut method for InSAR two-dimensional phase unwrapping," *IEEE Trans. Geosci. Remote Sens.*, vol. 60, 2022, Art. no. 5209615.

[34] L. Zhou, H. Yu, and Y. Lan, "Deep convolutional neural network-based robust phase gradient estimation for two-dimensional phase unwrapping using SAR interferograms," *IEEE Trans. Geosci. Remote Sens.*, vol. 58, no. 7, pp. 4653–4665, Jul. 2020.

[35] Y. Gao, G. Wang, G. Wang, T. Li, S. Zhang, S. Li, Y. Zhang, and T. Zhang, "Two-dimensional phase unwrapping method using a refined D-LinkNet-based unscented Kalman filter," *Opt. Lasers Eng.*, vol. 152, May 2022, Art. no. 106948.

[36] S. Vitale, G. Ferraioli, V. Pascazio, and G. Schirinzi, "InSAR-MONet: Interferometric SAR phase denoising using a multiobjective neural network," *IEEE Trans. Geosci. Remote Sens.*, vol. 60, 2022, Art. no. 5239814.

[37] Z. Wang, J. Wang, K. Yang, L. Wang, F. Su, and X. Chen, "Semantic segmentation of high-resolution remote sensing images based on a class feature attention mechanism fused with Deeplabv3+," *Comput. Geosci.*, vol. 158, Jan. 2022, Art. no. 104969.

[38] S. Woo, J. Park, and J. Lee, "CBAM: Convolutional block attention module," in *Proc. Eur. Conf. Comput. Vis. (ECCV)*, 2018, pp. 3–19.

[39] P. Wang, P. Chen, Y. Yuan, D. Liu, Z. Huang, X. Hou, and G. Cottrell, "Understanding convolution for semantic segmentation," in *Proc. IEEE Winter Conf. Appl. Comput. Vis. (WACV)*, Mar. 2018, pp. 1451–1460.
[40] R. G. Waghmare, D. Mishra, G. R. K. S. Subrahmanyam, E. Banoth, and S. S. Gorthi, "Signal tracking approach for phase estimation in digital holographic interferometry," *Appl. Opt.*, vol. 53, no. 19, pp. 4150–4157, 2014.

DONGXU LI was born in Shanxi, China, in 1997. He is currently pursuing the master's degree with the Guangxi University of Science and Technology. His current research interests include deep learning and phase unwrapping for wrapped interferograms.

XIANMING XIE (Member, IEEE) was born in Sichuan, China, in 1979. He received the Ph.D. degree from the Department of Electronic Engineering, University of Electronic Science and Technology of China (UESTC), Chengdu, China. His current research interests include synthetic aperture radar signal processing, microwave remote sensing for digital elevation models, and phase unwrapping with application in adaptive optics, speckle imaging, digital holographic microscopy (DHM), interferometric synthetic aperture radar (InSAR), and interferometric synthetic aperture sonar (InSAS).